Insights into the plasma-assisted fabrication and nanoscopic investigation of tailored MnO_2 nanomaterials

Reference:
Barreca Davide, Gri Filippo, Gasparotto Alberto, Altantzis Thomas, Gombac Valentina, Fornasiero Paolo, Maccato Chiara.- Insights into the plasma-assisted fabrication and nanoscopic investigation of tailored MnO_2 nanomaterials
Inorganic chemistry / American Chemical Society - ISSN 0020-1669 - 57:23(2018), p. 14564-14573
Full text (Publisher's DOI): https://doi.org/10.1021/ACS.INORGCHEM.8B02108
To cite this reference: https://hdl.handle.net/10067/1562450151162165141

Insights in the Plasma-Assisted Fabrication and Nanoscopic Investigation of Tailored MnO_2 Nanomaterials

Davide Barreca,[‡]* *Filippo Gri,*[†] *Alberto Gasparotto,*[†] *Thomas Altantzis,*[§] *Valentina Gombac,*[#] *Paolo Fornasiero,*[#] *and Chiara Maccato*[†]*

[‡] CNR-ICMATE and INSTM, Department of Chemical Sciences, Padova University, 35131 Padova, Italy.

[†] Department of Chemical Sciences, Padova University and INSTM, 35131 Padova, Italy.

[§] EMAT, University of Antwerp, 2020 Antwerp, Belgium.

[#] Department of Chemical and Pharmaceutical Sciences, ICCOM-CNR and INSTM, Trieste University, 34127 Trieste, Italy.

RECEIVED DATE (to be automatically inserted after your manuscript is accepted if required according to the journal that you are submitting your paper to)

ABSTRACT

Among transition metal oxides, MnO_2 is of considerable importance for various technological end-uses, from heterogeneous catalysis to gas sensing, owing to its structural flexibility and unique properties at the nanoscale. In this work, we demonstrate the successful fabrication of supported MnO_2 nanomaterials by a catalyst-free plasma-assisted process starting from a fluorinated manganese(II) molecular source in Ar/O_2 plasmas. A thorough multi-technique characterization aimed at the systematic investigation of material structure, chemical composition and morphology revealed the formation of F-doped, oxygen-deficient MnO_2-based nanomaterials, with a fluorine content tunable as a function of growth temperature (T_G). Whereas phase-pure β-MnO_2 was obtained for 100°C ≤ T_G ≤ 300°C, the formation of mixed phase MnO_2+Mn_2O_3 nanosystems took place at 400°C. In addition, the system nano-organization could be finely tailored, resulting in a controllable evolution from wheat-ear columnar arrays to high aspect ratio pointed-tip nanorod assemblies. Concomitantly, magnetic force microscopy analyses suggested the formation of spin domains with features dependent on material morphology. Preliminary tests in the Vis-light activated photocatalytic degradation of Rhodamine B aqueous solutions pave the way to possible applications of the target materials in wastewater purification.

KEYWORDS: MnO_2; plasma assisted-chemical vapor deposition; fluorine doping; magnetic force microscopy; photocatalysis.

INTRODUCTION

In the last decade, manganese oxides (MnO_x) have attracted a great interest due to their extremely diversified chemico-physical properties and wide range of potential applications.[1-6] In particular, MnO_2 is an inexpensive and environmentally friendly material characterized by a large natural abundance, rich polymorphism and high structural flexibility.[7-14] These features render MnO_2 an amenable multi-functional platform for a variety of utilizations, encompassing (photo)catalysis for water splitting and oxidation processes, chemical sensing, Li-ion batteries, electrochemical capacitors and magnetic devices.[6,13,15-29] Hence, attention has been devoted to the development of MnO_2 nanomaterials with controlled chemical, physical and functional properties.[1,15-16,30] In particular, one- and two-dimensional (1D, 2D) MnO_2 nanostructures have received an increasing attention due to their high surface area and tunable characteristics, dependent on dimensionality and size reduction.[4,7-8,14,20,31] The most used routes to fabricate morphology-controlled MnO_2 nanosystems are based on various liquid-phase approaches,[2,9,12,20,3210,15,17,25] that often require the use of complex reaction mixtures and/or long reaction times, preventing thus a large-scale utilization. In addition, most of the works carried out so far have been devoted to the fabrication of manganese dioxide powders, whereas the preparation of supported MnO_2 films and nanosystems, of importance for the eventual material integration into technological devices, has been comparatively less studied.[13,18-19,32] In this context, gas-phase processes like chemical vapor deposition, especially plasma-assisted (PA-CVD), hold a considerable promise thanks to the possibility of obtaining unique material morphology and structure under non-equilibrium conditions.[33-37] However, to the best of our knowledge, only three works on the plasma-assisted preparation of MnO_2[22,32] and MnO_x[33] nanosystems, with a difficult control of phase composition in the latter case, are available in the

literature up to date. Beside the adopted preparation route, a valuable method to manipulate MnO_2 chemico-physical characteristics involves also its controlled doping.[21,23,38] So far, various examples on cation-doped MnO_2 systems are present,[12,21,23] whereas the use of anionic dopants, such as fluorine, has never been reported. Interestingly, F introduction in the oxide network can not only affect the system composition and morphology, but also yield the passivation of surface defects, resulting thus in an enhanced electrical conductivity and higher Lewis acidity of the metal center, of utmost importance for energy storage, gas sensing and photocatalytic applications.[5,38-45] In particular in the latter field, defect passivation suppresses the undesired recombination of photogenerated charge carriers, an enhanced material conductivity favors electrons and holes migration towards surface adsorbates, whereas the increased Mn acidity improves the system reactivity. Hence, fluorine doping appears as a flexible and amenable tool to tailor the ultimate material performances.

Recently, we have carried out a study on the chemico-physical properties of the fluorinated complex $Mn(tfa)_2$•TMEDA (tfa = 1,1,1-trifluoro-2,4-pentanedionate; TMEDA = *N*,*N*,*N'*,*N'*-tetramethylethylenediamine) as PA-CVD precursor, and reported preliminary results on the obtainment of MnF_2 or MnO_2 systems under different reaction environments.[34] In this context, a thorough understanding of the interrelations between the processing conditions and the chemical, physical and functional properties of the developed systems is an open issue requiring further attention. With this background in mind, in the present manuscript we report on the successful PA-CVD fabrication of nanosystems based on β-MnO_2, the most thermodynamically stable polymorph of manganese dioxide.[31,46] So far, various works have been devoted to the preparation of this phase both in powdered forms[3,11-12,24] and as thin films,[18,32] but no previous investigation on the CVD preparation of β-MnO_2 films/nanosystems is available in the literature up to date. In

this study, we propose a single-step PA-CVD approach for the preparation and simultaneous *in-situ* F doping of manganese dioxide, involving the use of $Mn(tfa)_2$•TMEDA in Ar/O_2 plasmas at growth temperatures between 100 and 400°C. Under the adopted experimental conditions, this compound serves as a single-source molecular precursor for both Mn and F, thanks to the generation of fluorinated radicals.[40,45] The temperature influence is investigated in detail, devoting special attention to the possibility of tailoring not only the system structure and chemical composition, but also the nano-organization from columnar arrays to quasi-1D nanorod assemblies. In particular, the present study reports on a multi-technique nanoscopic investigation of nucleation/growth processes for β-MnO_2-based systems by means of advanced microscopic and spectroscopic techniques. Attention is also dedicated to the investigation of magnetic characteristics by magnetic force microscopy, performed for the first time on β-MnO_2 materials. Finally, the system photocatalytic performances are preliminarily evaluated in a standard test reaction, *i.e.* the liquid phase photodegradation of Rhodamine B (RhB) activated by Vis light.

EXPERIMENTAL SECTION

Synthesis. Depositions were performed using the $Mn(tfa)_2$•TMEDA precursor[34-35] on previously cleaned[40] *p*-type Si(100) substrates (MEMC®, Merano, Italy, 1.5 × 1.5 cm^2), mounted on the grounded electrode of a custom-built two-electrode radio frequency (RF, ν = 13.56 MHz) PA-CVD reactor[36] (electrode-to-electrode distance = 6.0 cm). Basing on preliminary optimization experiments, syntheses were carried out for 60 min from Ar/O_2 plasmas (flow rates = 15.0 and 5.0 standard cubic centimeters per minute (sccm), respectively), using a total pressure of 1.0 mbar and an RF-power of 20 W. The used growth temperature (T_G) was varied between 100 and 400°C. $Mn(tfa)_2$•TMEDA powders, introduced in an external glass reservoir, were heated at

85°C by means of an oil bath and their vapors were transported into the reactor by an additional Ar flow (60 sccm) through delivery gas lines maintained at 150°C. The obtained samples were analyzed as-prepared, without any *ex-situ* thermal treatment, in order to prevent MnO_2 thermal decomposition.[32]

Characterization. X-ray photoelectron spectroscopy (XPS) analyses were performed by a Perkin–Elmer Φ 5600ci spectrometer, using a standard AlKα source (hν = 1486.6 eV). The obtained binding energy (BE) values (uncertainty = ±0.2 eV) were corrected for charging effects by assigning to the adventitious C1s component a value of 284.8 eV.[6] Ar^+ sputtering was carried out at 4.0 kV, with an Ar partial pressure of 5×10^{-8} mbar. When necessary, peak fitting was performed by a least-squares procedure using Gaussian–Lorentzian peak shapes. Atomic percentages (at.%) were determined through peak integration using Φ V5.4A sensitivity factors.

X-ray diffraction (XRD) patterns were collected at an incidence angle of 1.0° using a Bruker D8 Advance diffractometer equipped with a Göbel mirror and a CuKα X-ray source.

Field emission-scanning electron microscopy (FE-SEM) images were acquired using a Zeiss SUPRA 40VP instrument, equipped with an Oxford INCA x-sight X-ray detector for energy dispersive X-ray spectroscopy (EDXS) analyses, at primary electron beam voltages of 10-20 kV. The mean nanodeposit thickness and nanoaggregate dimensions were estimated using the ImageJ® software (http://imagej.nih.gov/ij/).

The material surface topography and magnetic properties were investigated by atomic and magnetic force microscopies (AFM and MFM), using a NT–MDT SPM Solver P47H–PRO instrument operating in tapping mode and in air. Root mean square (RMS) roughness values were calculated from AFM images by means of the NT-MDT software after background subtraction. MFM analyses were performed using cantilever tips (mean height = 15 μm) coated

with a CoCr magnetic film (thickness = 15 nm) on the tip side and by a high-reflectivity Al coating on the detector side. Before image acquisition, the tips were magnetized for 60 min.

Cross-sectional samples for transmission electron microscopy (TEM) observations were prepared by focused ion beam (FIB-SEM, FEI HELIOS Nanolab 650), as well as by Ar^+ ion milling. In the latter case, specimens were first mechanically polished down to a thickness of approximately 20 μm using an Allied Multiprep System with diamond-lapping films, and, subsequently, subjected to Ar^+ ion milling using a Leica EM RES102 apparatus. During the preparation of the sample grown at 400°C, characterized by the presence of long nanorods with a relatively low packing density (see below), a carbon coating and a Pt protective layer (high contrast regions between the rods) were deposited to embed the structures and prevent them from collapsing. Low and high magnification high angle annular dark field-scanning TEM (HAADF-STEM) images, selected area electron diffraction (SAED) patterns and EDXS elemental maps were acquired using an aberration corrected cubed FEI Titan electron microscope operated at 300 kV, equipped with the ChemiSTEM system.[47] A probe convergence semi-angle and a detector collection inner semi-angle of 21 mrad and 55 mrad, respectively, were used for image acquisition.

The photocatalytic activity was tested in the degradation of RhB aqueous solutions using a 30 mL teflon photochemical reactor. In a typical experiment, a β-MnO_2 catalyst was immersed in 20 mL of the dye solution (initial concentration = 2.0×10^{-6} M), stirred in the dark for 30 min in order to reach the adsorption equilibrium. Under these conditions, the maximum decrease in the dye concentration was lower than 1 % for all the investigated samples. Subsequently, irradiation was performed using a Solar Simulator (LOT-Oriel) equipped with a 150 W Xe lamp, using a cut-off filter (AM-79765) to obtain the sole Vis irradiation. At different time intervals, 1.5 mL of

the aqueous suspension were collected and analysed by a UV-Vis spectrophotometer (Shimadzu UV-2450). The photocatalytic activity was evaluated by monitoring the decrease of the absorption band of RhB at λ = 553 nm as a function of time. The residual dye content was calculated as $A/A_0 \times 100$, where A and A_0 indicate the actual and reference absorbance values, respectively. Control experiments revealed that RhB was not decomposed under irradiation in the absence of manganese oxides, indicating that dye degradation was a photocatalytic process promoted by the target nanosystems.

RESULTS AND DISCUSSION

The surface chemical composition and elemental states of the fabricated samples were examined by XPS. Irrespective of the adopted growth temperature, only Mn, O, F and C peaks could be observed in survey scans (see Figure 1a and Supporting Information (SI), Figure S1a). The disappearance of carbon after Ar^+ erosion for 10 min evidenced the high material purity. The F1s signal (Figure 1a, inset; Figure 1b and SI, Figure S1b) could be always fitted by means of two different components. The low BE band (I, BE = 684.8 eV) was ascribed to lattice fluorine substitutional to oxygen atoms in the oxide network, whereas the high BE one (II, BE = 688.5 eV) was attributed to undecomposed CF_x precursor residuals.[5,34,39-40,45] Similarly to the carbon signal, the latter band was reduced to noise level after 10 min of Ar^+ erosion (see SI, Figure S1b), indicating that the presence of contaminating fluorine species was limited to material surface. Conversely, lattice F (component (I)) was present both on the material surface (Figure 1c) and in the inner system region (SI, Figure S1b). Interestingly, fluorine loading could be tailored by variations of the sole deposition temperature, whose increase resulted in a progressive decrease of both the total fluorine content and lattice one [component (I)], the latter disappearing

for T_G = 400°C (Figures 1b-c).

The present data highlight the successful fluorine incorporation in the target systems, thanks to the

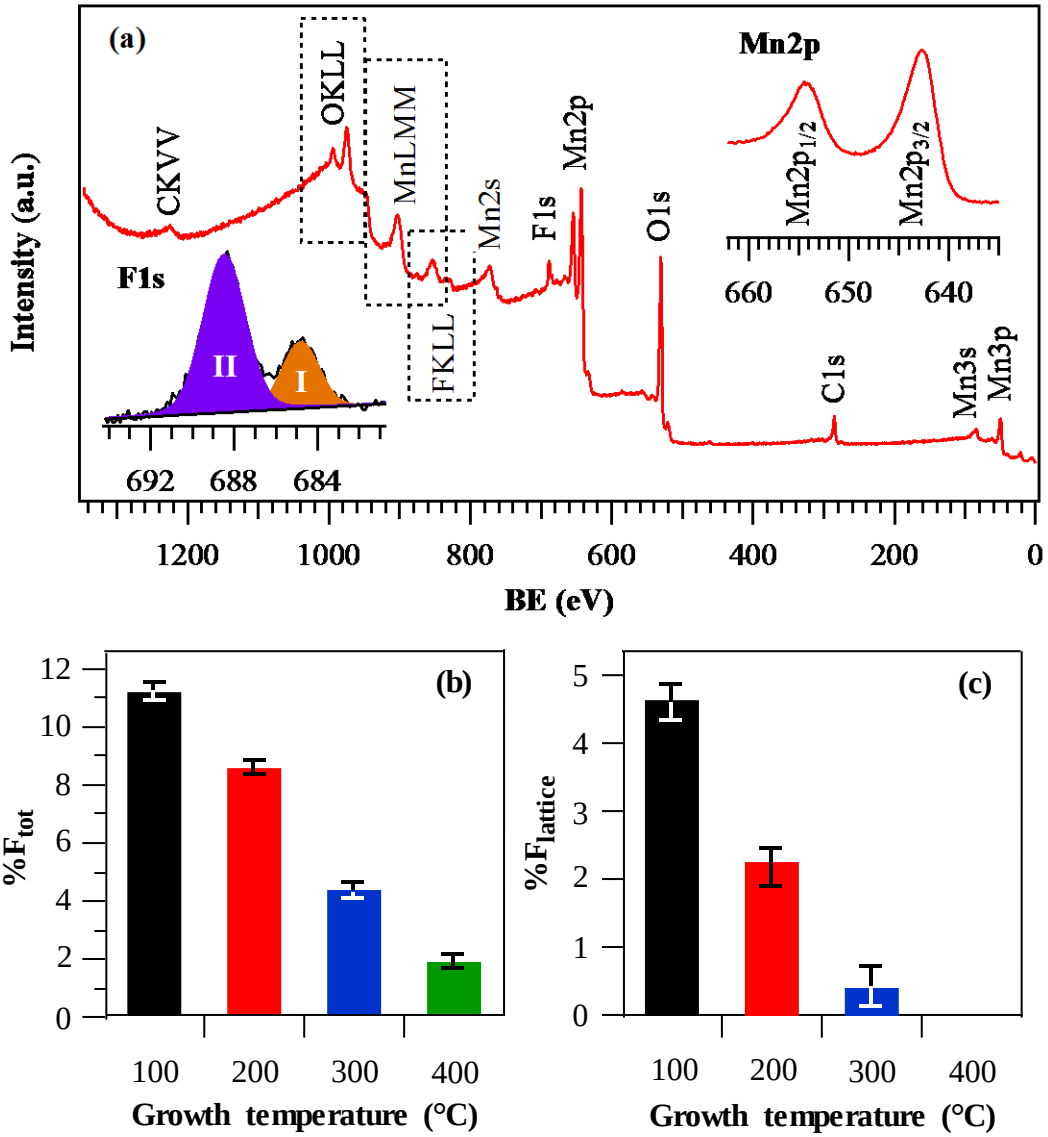

Figure 1. (a) Surface wide-scan XPS spectrum of a manganese oxide deposit synthesized at T_G = 200°C. The corresponding F1s and Mn2p photopeaks are displayed as insets. Dependence on growth temperature of the surface total F content (b) and lattice fluorine content (c).

use of the above mentioned fluorinated compound as PA-CVD precursor. The obtainment of fluorine doping, already reported in the PA-CVD growth of iron and cobalt oxide nanosystems from $M(hfa)_2$•TMEDA derivatives (M = Fe, Co; hfa = 1,1,1,5,5,5-hexafluoro-2,4-pentanedionate)[40,45,48-49] similar to the present $Mn(tfa)_2$•TMEDA precursor, was traced back to the generation of F• radicals from the diketonate ligand fragmentation in the used plasmas. The adsorption of these radicals onto the growing material results in F incorporation into the target system.[48] The trend in fluorine concentration (see Figures 1b-c) could be explained taking into account that, at the lowest temperatures, the adsorption of the above radicals is more efficient. This phenomenon is also accompanied by the binding of CF_x precursor residuals, but, as already observed, their presence is confined to material surface. Upon increasing T_G, the higher thermal energy supply triggers the formation of F-containing volatile byproducts, ultimately leading to the disappearance of lattice fluorine signals at a temperature of 400°C.

As regards Mn chemical state, the Mn2p signal shape and position (Figure 1a, inset and SI, Figure S1c; BE($Mn2p_{3/2}$) = 642.7 eV; spin-orbit separation = 11.6 eV) were in line with literature data for pure Mn(IV) oxide.[27] Nevertheless, since the distinction of the various Mn oxides based on the sole analysis of the Mn2p peak might be ambiguous,[23] the Mn3s core level spectrum was also collected (SI, Figure S1d).[33] The Mn3s multiplet splitting separation (≈4.8 eV, irrespective of the deposition temperature) confirmed indeed the occurrence of the sole Mn(IV) valence state[1,26] for all the analyzed specimens. Calculation of the O/Mn ratio (see also the O1s signal, SI, Figure S1e) yielded a mean value of 1.7, lower than the one expected for stoichiometric MnO_2, suggesting thus the occurrence of oxygen vacancies. The presence of the latter, already reported in various studies on the β-MnO_2 polymorph, has been reported to beneficially impact on MnO_2 catalytic and electrochemical activity.[11,16-17]

In this work, particular attention was devoted to the system structural and morphological characterization as a function of the adopted processing conditions by the combined use of complementary analytical techniques. The system structure was initially investigated by XRD (Figure 2a), and the obtained patterns revealed a marked dependence on the adopted deposition

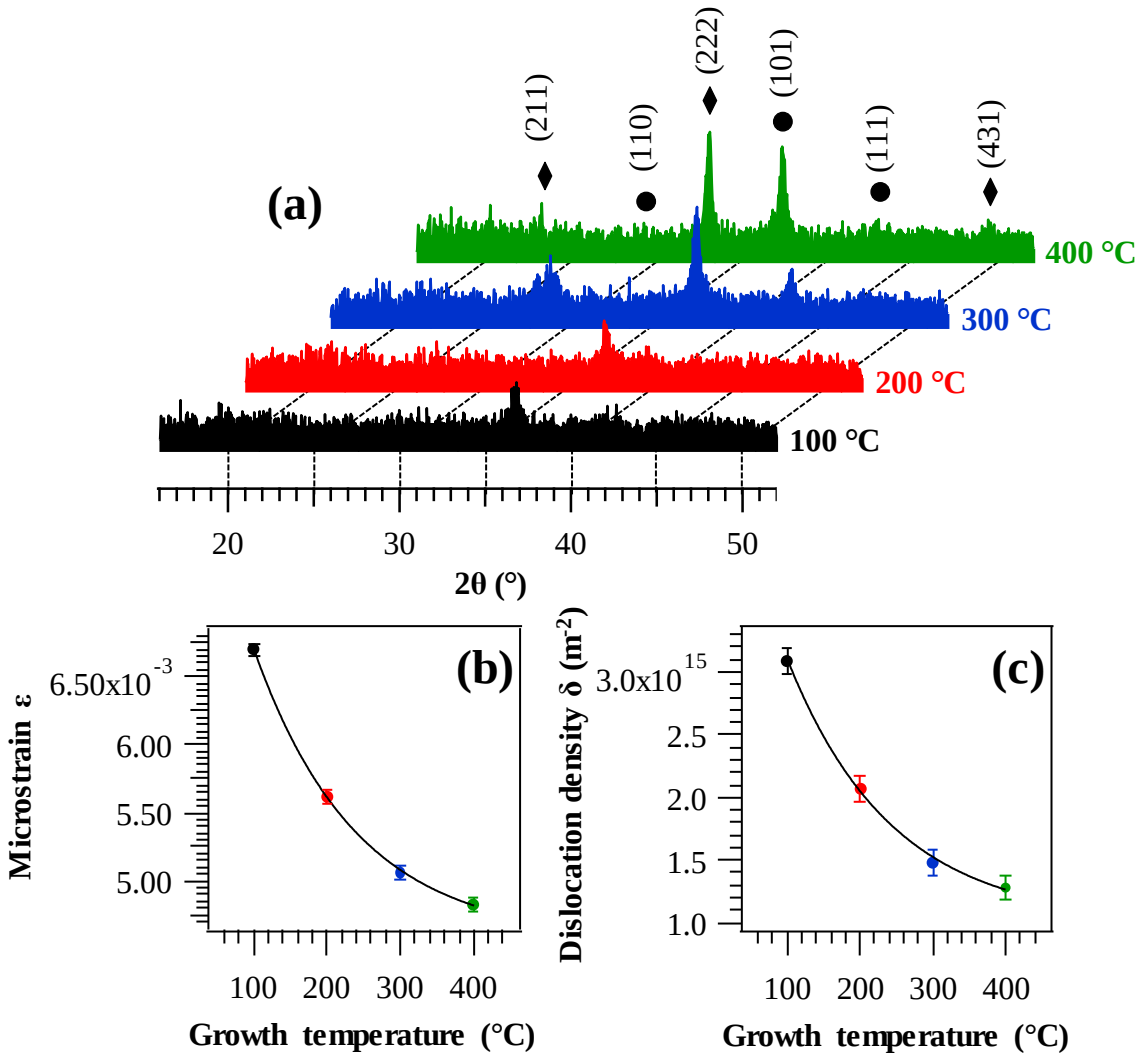

Figure 2. (a) XRD patterns of manganese oxide specimens deposited at various temperatures. β-MnO_2[50] and α-Mn_2O_3[51] reflections are marked by symbols ● and ♦, respectively. Dependence of the sample microstrain (b) and dislocation density (c) on the growth temperature.

temperature. As can be observed, crystalline deposits could be obtained at T_G as low as 100°C, an appreciably lower temperature than those used in the molecular beam epitaxy and the atomic

layer deposition of MnO_2 films,[22,32] as well as in the thermal CVD of Mn fluorides and oxides from an analogous diketonate-diamine Mn(II) precursor, thanks to the unique activation exerted by cold plasmas.[34] For $T_G \leq 200$°C, the recorded patterns showed a single diffraction peak, attributable to the (101) crystallographic planes of tetragonal β-MnO_2 (space group: $P4_2/mnm$; a = 4.399 Å, c = 2.874 Å).[4,24,50] β-MnO_2, the most thermodynamically stable manganese (IV) oxide polymorph under ambient conditions, possesses a rutile-type structure, characterized by MnO_6 octahedra linked along edges to form chains, which, in turn, connect *via* corner sharing yielding a tunneled structure.[2,8,10,46] The absence of the (110) signal at $2\theta \approx 28.7°$, the most intense one in the reference β-MnO_2 pattern,[50] suggested the possible occurrence of preferential orientations and/or anisotropic crystallite growth (see also FE-SEM data below).[34,39] At T_G = 300°C, the reflections at 2θ = 28.8°, 37.3° and 42.8° were assigned to (110), (101) and (111) planes of β-MnO_2. No signal pertaining to other crystalline phases could be observed, evidencing, for 100°C $\leq T_G \leq$ 300°C, the formation of phase-pure β-MnO_2 systems, at variance with previous results obtained in the PA-CVD of MnO_x thin films.[33] The $I_{(110)}/I_{(101)}$ intensity ratio was reversed with respect to the powder spectrum,[50] suggesting even in this case the presence of texturing effects and/or anisotropic growth. A similar observation held also for the specimen prepared at T_G = 400°C, in which the (110) β-MnO_2 peak could not be detected. In this case, however, the system phase composition turned out to be different. In fact, the pattern also revealed the presence of diffraction signals at 2θ = 23.2°, 33.1° and 49.4°, related to (211), (222) and (431) planes of α-Mn_2O_3,[51] whose formation could be ascribed to a partial MnO_2 thermal decomposition at the adopted growth temperature.[32] These results indicated that the temperature window useful to obtain pure β-MnO_2 under the present experimental conditions corresponds to 100°C $\leq T_G \leq$ 300°C. The apparent discrepancy between XRD and surface XPS results, which

showed the presence of the sole MnO_2 for T_G = 400°C, suggested that Mn_2O_3 was confined in the inner material regions close to the substrate, as confirmed by TEM data (see below). The average MnO_2 nanocrystal size *D* underwent a progressive increase with the deposition temperature (SI, Figure S2).

In general, the relatively low peak intensity and the line broadening in the XRD patterns of the target materials suggested a low system crystallinity. This phenomenon, already observed in the liquid phase synthesis of MnO_2 powders,[8-9,32] could be mainly related to the structural disorder induced by fluorine introduction in the fabricated systems, especially for T_G = 100°C.[38] In fact, a careful analysis of XRD data revealed a progressive shift of the (101) β-MnO_2 reflection towards lower angular values upon decreasing T_G. This effect could be traced back to the parallel increase of fluorine content (Figure 1), resulting in a strain of the lattice structure[41-44] and in a (101) peak location at $2\theta = 36.7°$, ≈0.6° lower than the reference β-MnO_2 value.[50] In any case, the absence of peaks related to secondary F-containing phases proved a successful fluorine insertion in the oxide lattice.[38] It is worth highlighting that the low crystallinity and high defectivity of the present materials, resulting in a high density of surface active sites, could be in principle advantageous in view of (photo)catalytic applications, such as the removal of dyes from aqueous solutions and the oxygen evolution reaction.[2-3]

Additional important information was provided by the calculation of microstrain (ε) and dislocation density (δ) values (SI, § S-1.2). For both these parameters, Figures 2b-c evidenced an exponential decrease upon increasing the deposition temperature, suggesting that an enhanced thermal energy supply resulted in a lowered defect content and a higher material crystallinity.[41-42] The obtained δ values were similar to those reported for manganese oxide systems with similar crystallite dimensions (see also SI, Figure S2).[14,39]

In order to investigate in detail the system nano-organization, both plane-view and cross-sectional FE-SEM analyses were performed, and the results revealed a remarkable dependence of material morphology on the adopted growth temperature (Figure 3). The specimen fabricated at 100°C was characterized by densely interconnected wheat-ear shaped structures growing almost perpendicularly to the substrate surface (mean height = (320±10) nm). As a result, a surface

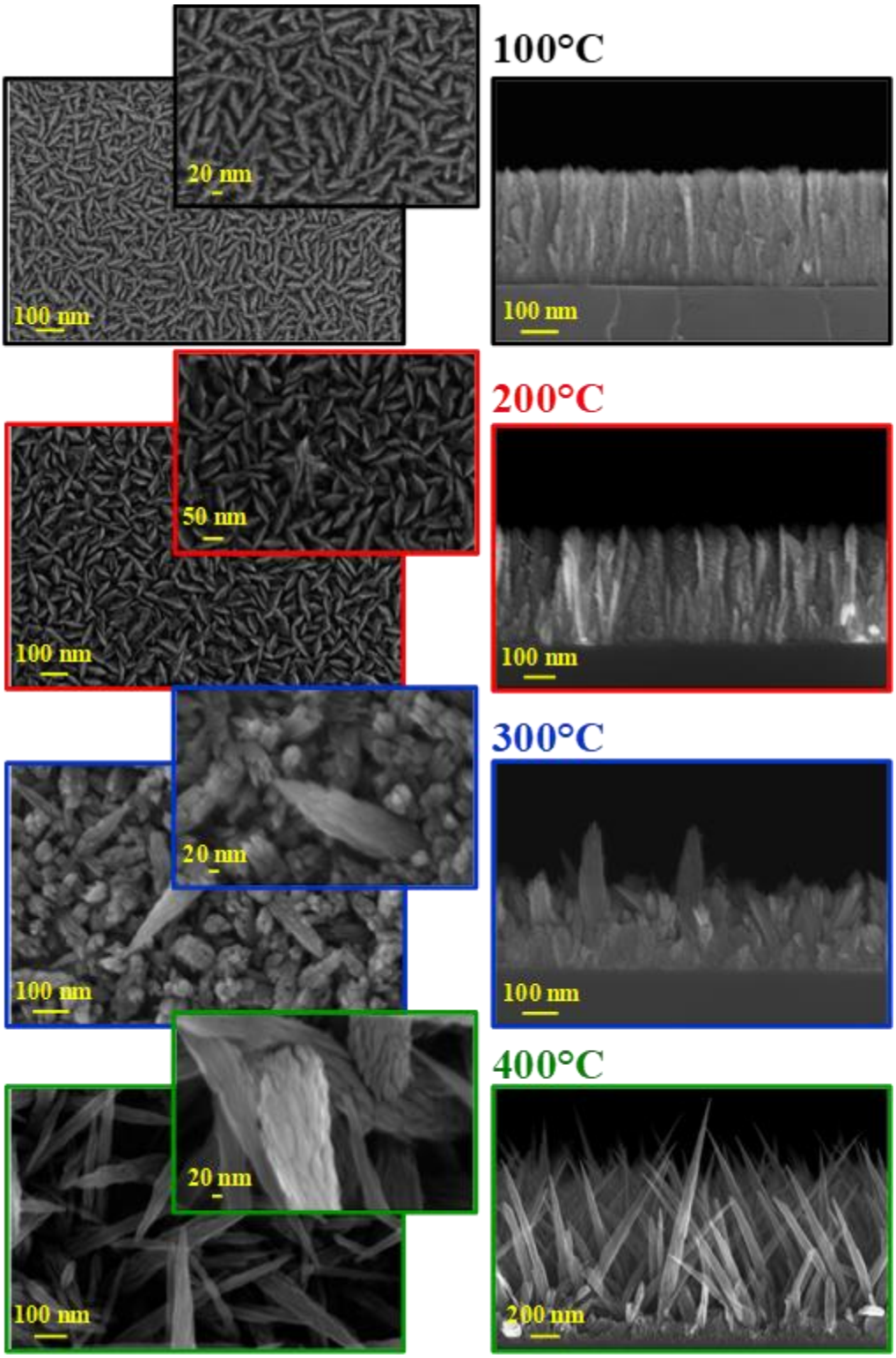

Figure 3. Plane-view (left) and cross-sectional (right) FE-SEM micrographs for samples synthesized at different temperatures.

topography dominated by the uniform interconnection of evenly distributed lamellar aggregates could be observed (lamellae length and width = (80±15) nm and (25±5) nm, respectively). For T_G = 200°C, the deposit was less compact and the mean height of nanostructures increased to (370±20) nm. In a different way, the specimen prepared at 300°C presented elongated aggregates (average length up to ≈400 nm; diameter = (70±10) nm) outgrowing from a relatively compact granular underlayer in contact with the Si(100) substrate. The presence of the latter was observed even at T_G = 400°C, but in this case the images revealed the formation of outgrowing pointed-tip nanorods (length ≈ 1050 nm; diameter = (70±20) nm; aspect ratio = length/diameter = 15), whose assembly gave rise to the formation of a highly porous material.

The obtained MnO_2-based nanosystems were further investigated by means of cross-sectional EDXS analyses, carried out in parallel to FE-SEM ones. The corresponding results (SI, Figure S3) revealed a homogeneous in-depth composition, without the presence of any impurity, in accordance with XPS data, and an even fluorine distribution throughout the investigated thickness.

The joint use of AFM and MFM enabled to analyze the surface topography and the corresponding distribution of magnetic domains in the target nanomaterials. Figure 4 displays AFM (left) and MFM images (right), both revealing an appreciable evolution as a function of the growth temperature. In line with FE-SEM results, AFM analyses highlighted the progressive formation of rougher surfaces at higher T_G values, with a less regular surface topography for T_G = 300 and 400°C, in line with the evolution towards pointed-tip nanorods (see Figure 3). In particular, RMS roughness values were evaluated to be 1, 4, 44 and 50 nm for T_G = 100, 200, 300 and 400°C, respectively (SI, Figure S4). Especially in the latter case, the resulting highly porous morphology has a great potential interest for technological applications requiring a high

surface area, such as gas sensing and photocatalysis (see below).[7,49] It is worthwhile noting that the direct measurement

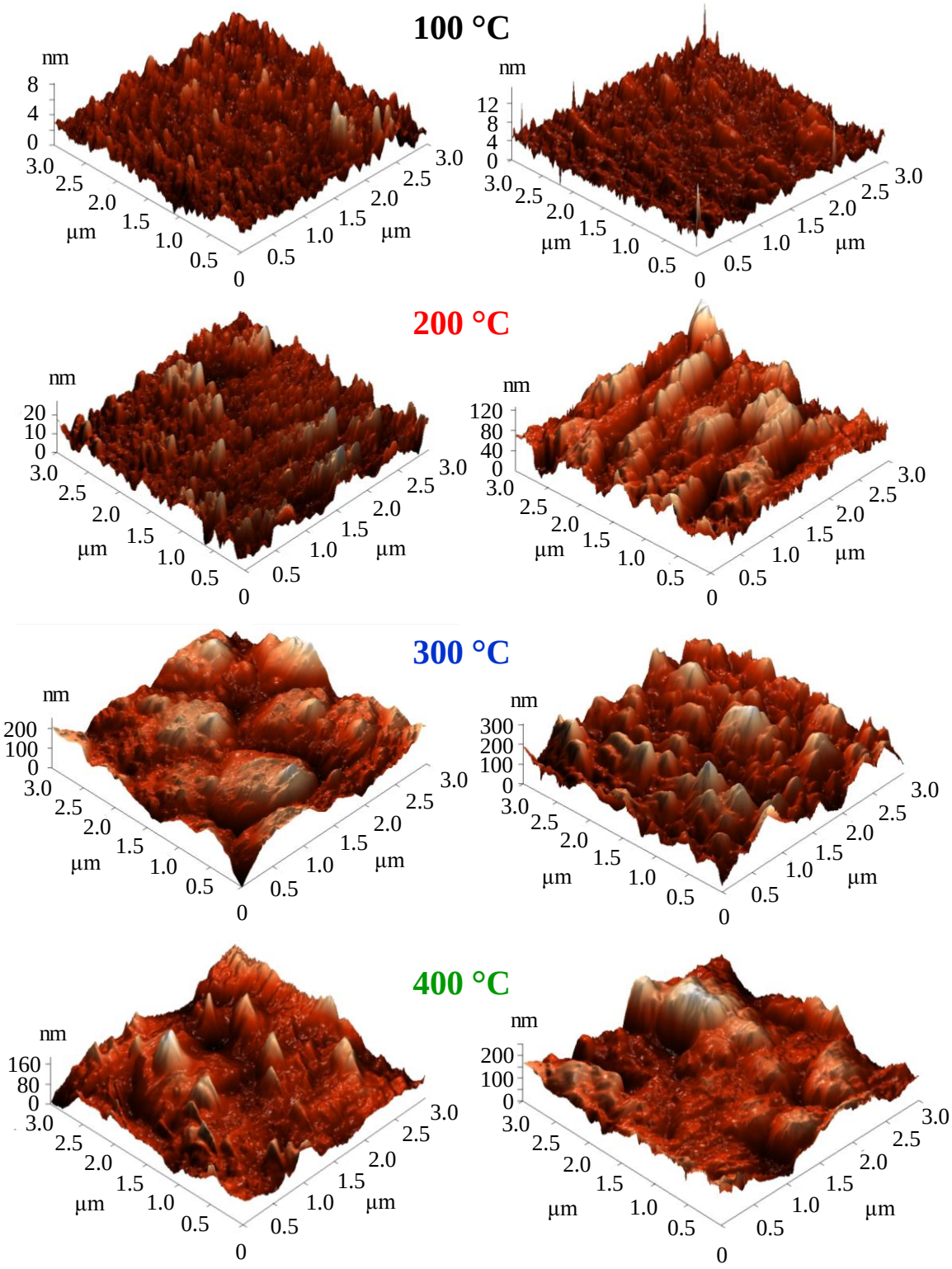

Figure 4. Topographic AFM images (left) and MFM micrographs (right) for manganese oxide specimens obtained at different growth temperatures.

of surface area values for supported nanosystems like the present ones is indeed a critical issue. In fact, in such cases conventional N_2 or Kr physisorption methods fail, as the extremely low mass of the active material cannot be estimated with accuracy.[37] In this regard, Root Mean Square (RMS) roughness values obtained by AFM measurements provide valuable information, since the effective surface area is typically larger for a rough surface[45] and therefore the RMS values display the same trend as the surface area ones.

MFM images (Figure 4) showed domain structures reflecting the magnetic polarization at the top end of nanoaggregates. The magnetic properties shown by the developed manganese oxide materials could be related to the presence of oxygen vacancies,[22] in line with XPS data (see above). A careful analysis of morphological data revealed that the dimensions of magnetic domains sampled by MFM were different from those of the aggregates in AFM and FE-SEM micrographs, especially for T_G > 300°C. This evidence suggested that each of the observed domain comprises various aggregates with a very close alignment. For 100°C ≤ T_G ≤ 300°C, the relatively uniform distribution of bright/dark regions, corresponding to a higher local concentration of positive/negative poles,[52] revealed a long-range magnetic ordering. A different situation was observed at 400°C, due to the above observed quasi-1D anisotropic morphology. Indeed, since the magnetic tip used to probe material surface is sensitive to the force gradient perpendicular to in-plane magnetic domains, the corresponding MFM image suggested the occurrence of a perpendicular magnetic anisotropy, of potential interest for an eventual end-use of the developed materials in high-density magnetic recording media.[53] Furthermore, the topography at T_G = 400°C reflected a bunching/bundling of quasi-1D structures, which was ascribed to the inability of the magnetic tip to spatially resolve individual nanorods.

In order to investigate in detail the system nanoscale structure, HAADF-STEM and EDXS

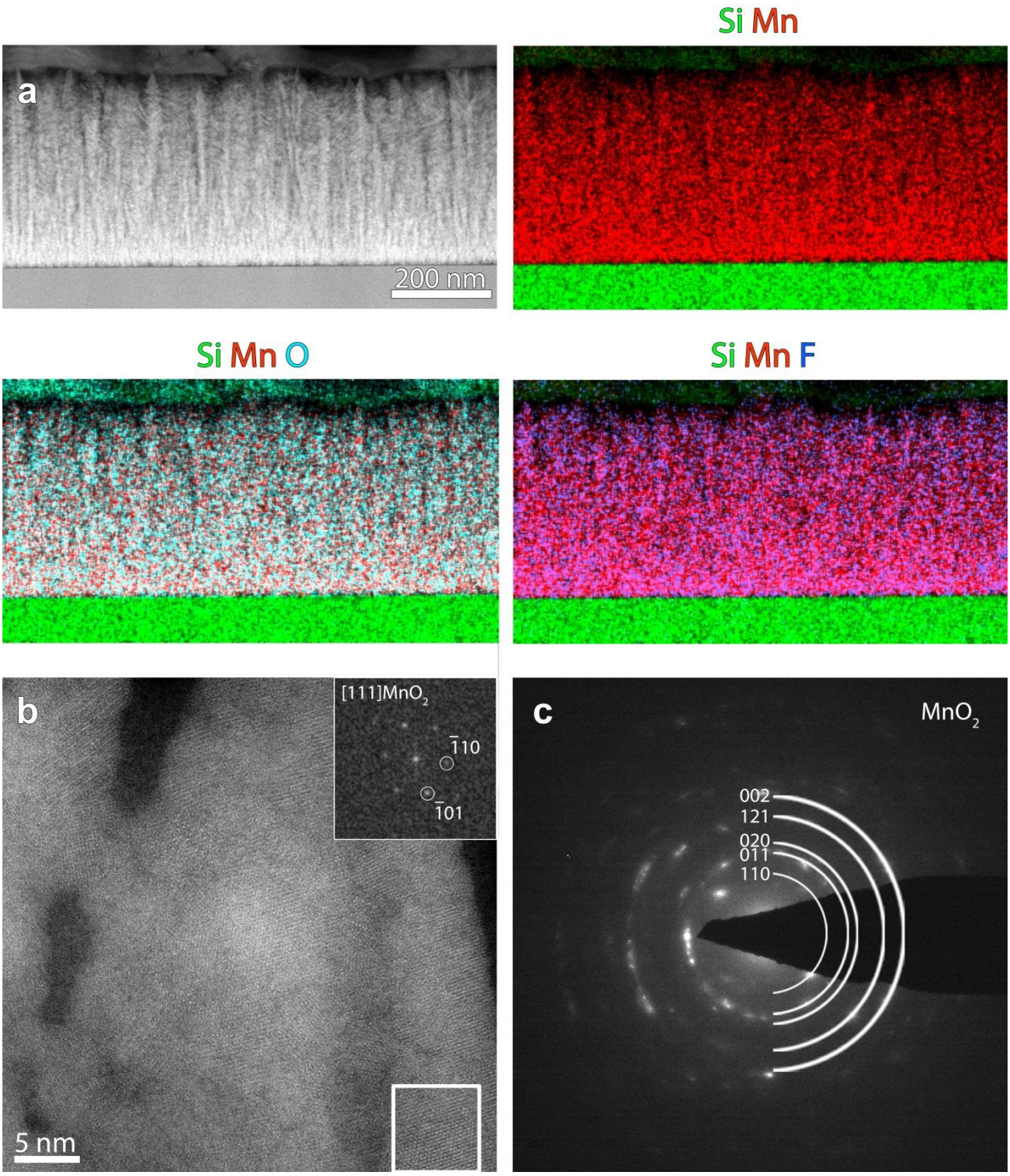

Figure 5. (a) Cross-sectional HAADF-STEM image and corresponding EDXS elemental maps for the sample fabricated at T_G = 200°C. (b) High resolution STEM image from the same specimen together with the FFT pattern of the region marked by the white square. The crystal is oriented along the [111] axis of the β-MnO_2 structure. (c) SAED pattern from a region in (a).

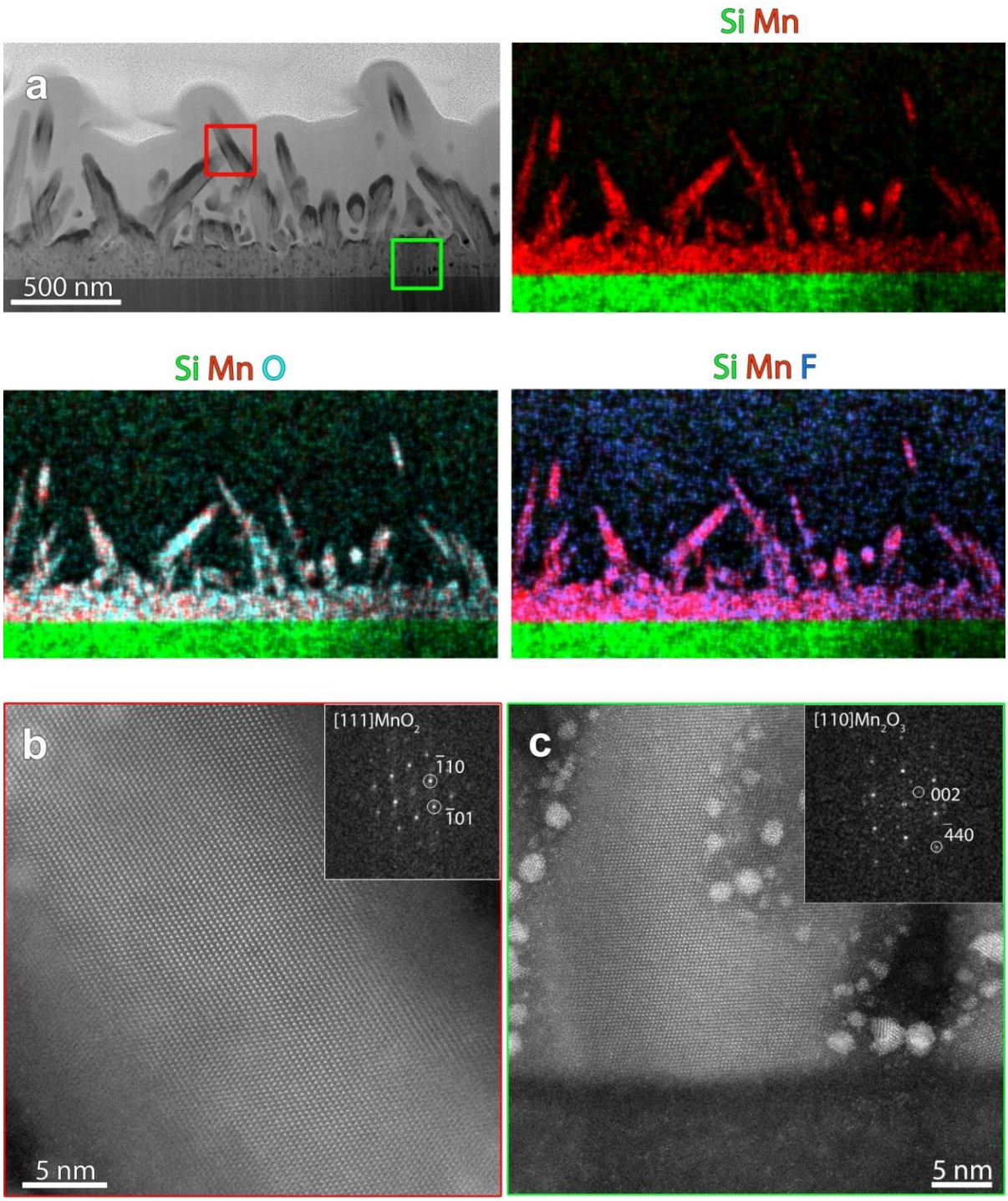

Figure 6. (a) Cross-sectional HAADF-STEM image and corresponding EDXS elemental maps for the specimen fabricated at T_G = 400°C. (b,c) High resolution STEM images for the grown needles and the underlayer, corresponding to the regions marked by red and green squares marked in (a). FFT patterns (shown as insets) indicate that the structure of the needles and of the underlayer corresponds to β-MnO_2 and α-Mn_2O_3, respectively. In Figure 6c, high contrast Pt nanoparticles from the protective layer used during sample preparation are clearly evident.

analyses were carried out on two representative specimens fabricated at T_G = 200°C (Figure 5) and 400°C (Figure 6). An overview HAADF-STEM image of the sample grown at T_G = 200°C, together with EDXS elemental maps for Si, Mn, O and F, are shown in Figure 5a. Beside revealing the Si//MnO_2 stacking and a uniform element spatial distribution, the results evidenced the presence of columnar structures, in agreement with FE-SEM observations (compare Figure 3). Figure 5b displays a high resolution HAADF-STEM (*Z*-contrast) micrograph, together with the fast Fourier transform (FFT) pattern of the crystal indicated by the white square, shown as inset. The FFT corresponds to the [111] zone axis of β-MnO_2,[50] the sole polymorph detected in the present specimen, in line with XRD data (see above and Figure 2a). The circles observed in SAED analysis (Figure 5c) highlighted the polycrystalline nature of the target system. Figure 6a reports an overview HAADF-STEM image of the sample fabricated at T_G = 400°C, along with EDXS elemental maps. The micrographs evidenced the assembly of quasi-1D high aspect ratio nanorods with pointed tips, outgrowing from a relatively compact underlayer in contact with the FTO substrate. Figures 6b-c display representative high resolution HAADF-STEM images for the target nanorods and the underlayer, collected in the regions marked in Figure 6a by red and green squares, respectively. The corresponding FFT patterns showed that the nanorod structure corresponded to β-MnO_2,[50] whereas the underlayer was composed by the sole α-Mn_2O_3, in agreement with XRD analyses that revealed the co-presence of β-MnO_2 and α-Mn_2O_3 at T_G = 400°C.

As a whole, the above results enabled us to propose a tentative growth mechanism involving a thermally activated vapor-solid auto-catalytic process (see Figure 7). In particular, the formation of the first nucleation centers during the initial deposition stages is followed by their coalescence into a granular coating in contact with the substrate, acting as a ‘seed layer’ and triggering the

subsequent material development. Accordingly, an anisotropic grain growth yields the formation

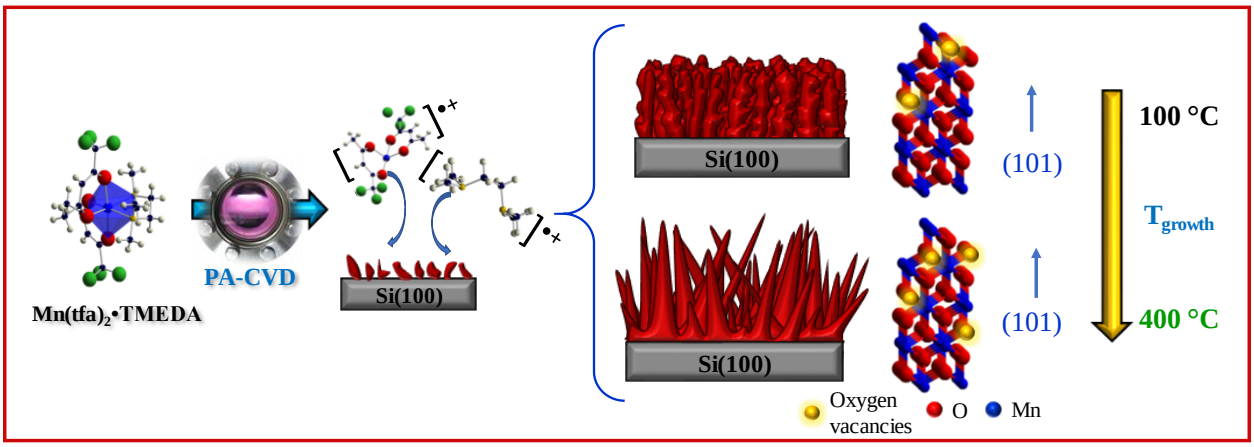

Figure 7. Schematic representation of the various steps involved in the PA-CVD growth of manganese oxide nanomaterials on Si(100) substrates in the 100–400°C temperature range.

of nanostructures mainly oriented along the (101) crystallographic direction. As a matter of fact, this phenomenon is directly affected by the actual temperature of the growth surface, governing not only the level of fluorine incorporation (see above and Figure 1), but also the nature of the ultimate products. In fact, whereas at the lowest adopted temperatures (100 and 200°C) compact columnar arrays are observed, a progressive increase in the thermal energy supply ($T_G \geq 300$°C) is responsible for the progressive formation of more open and porous structures. The use of T_G = 400°C promotes a quasi-1D growth, yielding β-MnO_2 pointed-tip nanorods protruding from an underlayer composed by α-Mn_2O_3.

Finally, a preliminary proof-of-principle investigation of material photocatalytic activity was carried out in the Vis-light photodecomposition of aqueous RhB solutions.[8,29] Figure 8 displays the relative RhB concentration *vs*. illumination time in the presence of selected manganese oxide nanosystems prepared at the lowest and highest substrate temperatures (100 and 400°C, respectively). As can be observed, RhB was progressively degraded under Vis irradiation, and

the

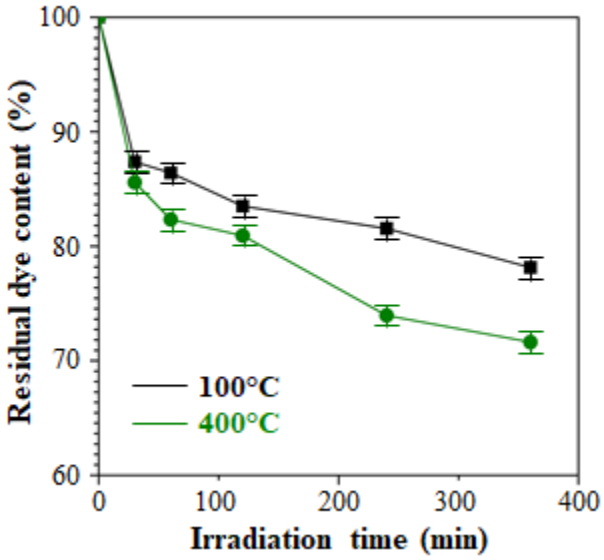

Figure 8. Photocatalytic degradation of RhB aqueous solutions (2×10^{-6} M) under Vis light in the presence of selected MnO_2 specimens.

system performances were directly affected by the material deposition temperature. Although the presence of Mn_2O_3 and the concomitant formation of Mn_2O_3/MnO_2 heterojunctions in the specimen prepared at 400°C (see above) might be unfavorable for the separation of photogenerated electrons and holes,[8,54] the decomposition efficiency was higher for the sample grown at 400°C with respect to the homologous one obtained at 100°C. This phenomenon could be mainly related to contributions from the system surface roughness (a higher roughness likely corresponding to a higher active area[45]), which was 50 times higher for the 400°C sample with respect to the 100°C one (see above and SI, Figure S4). In addition, the system functional performances could be directly affected by the fluorine content. In particular, as can be observed in Figures 1b-c, the overall fluorine percentage progressively decreased upon increasing the growth temperature. Since a main contribution to the overall F content arose from undecomposed

CF_x precursor residuals (compare Figure 1a), it can be deduced that especially at T_G = 100°C the latter moieties, present at material surface, exert a poisoning effect on the catalyst, resulting in a decreased activity towards dye degradation and accounting for the diverse sample performances reported in Figure 8.[45] In this regard, the independent control of lattice *vs*. contaminating F content undoubtedly deserves further attention. Nevertheless, it is worthwhile highlighting that the preparation route proposed in the present study enables the obtainment of nanosystems with a minimal amount of active material, much lower than the typical ones for homologous powdered specimens. In addition, supported nanosystems like the present ones are an amenable alternative for practical uses, since their adhesion to the substrate prevents the occurrence of unfavorable leaching/sintering phenomena affecting powdered systems.

CONCLUSIONS

In summary, supported MnO_2 nanomaterials with tailored nano-organization were fabricated for the first time through a PA-CVD route starting from a fluorinated Mn(II) derivative in Ar/O_2 plasmas. Key points of the proposed approach are: i) the lower processing temperatures with respect to those previously adopted in the thermal CVD of manganese oxides/fluorides and in the molecular beam epitaxy/atomic layer deposition of MnO_2 systems; ii) the absence of catalysts and/or templating agents, resulting in high purity products. In particular, this investigation has unraveled the interrelations between the processing conditions and the system structural, compositional, morphological properties. The versatility of the adopted strategy, which represents an amenable alternative for possible large-scale applications, is highlighted by the possibility of controlling material characteristics by the sole variation of the growth temperature from 100 to 400°C. In particular, fluorine content could be finely modulated, and material phase

composition changed from pure β-MnO_2, for $100 \leq T_G \leq 300$°C, to a mixed phase MnO_2+Mn_2O_3 system, for $T_G = 400$°C. In parallel, the system morphology underwent an evolution from wheat-ear arrays to quasi-1D assemblies, accompanied by a progressive increase of the surface roughness and by variations in the shape and distribution of the resulting magnetic domains. Preliminary photocatalytic results evidence that the target β-MnO_2 systems are suitable for RhB degradation under Vis light.

The obtained results provide a general framework on how to control the system morphogenesis for advanced technological applications not only in magnetic recording media, but also in gas sensors and (photo)catalysts for oxygen evolution. In this regard, future efforts will be addressed to a wider screening of processing conditions to verify the possibility of exerting an independent control of lattice *vs*. contaminating fluorine in the prepared materials.

AUTHOR INFORMATION

Corresponding Authors

* Tel: +39-049-8275170; E-mail: davide.barreca@unipd.it; ORCID: 0000-0002-8779-3386 (D.B.). Tel: +39-049-8275234; E-mail: chiara.maccato@unipd.it; ORCID: 0000-0001-6368-5754 (C.M.).

Author Contributions

The manuscript was written through the contributions of all the authors. All the authors have given their approval to the final manuscript version.

Notes

The authors declare no competing financial interest.

ACKNOWLEDGEMENTS

The present work was financially supported by Padova University DOR 2016–2018 and P-DiSC #03BIRD2016-UNIPD projects. T.A. acknowledges a post-doctoral grant from the Research Foundation Flanders (FWO). Thanks are also due to Prof. Sara Bals (EMAT, University of Antwerp, Belgium) and to Dr. Giorgio Carraro (Department of Chemical Sciences, Padova University, Italy) for valuable support and experimental assistance.

ASSOCIATED CONTENT

Supporting Information. XPS surveys, Mn2p and Mn3s spectra for all the analyzed specimens; fitted F1s and O1s photopeaks and pertaining comments; further details on XRD analyses (average nanocrystal dimensions, microstrain, dislocation density); EDXS results; AFM roughness data. This material is available free of charge via the Internet at http://pubs.acs.org.

REFERENCES

(1) Wang, J. F.; Zhang, G. N.; Ren, L. J.; Kang, L. P.; Hao, Z. P.; Lei, Z. B.; Liu, Z. H. Topochemical Oxidation Preparation of Regular Hexagonal Manganese Oxide Nanoplates with Birnessite-Type Layered Structure. *Cryst. Growth Des.* **2014**, *14*, 5626-5633.

(2) Liu, Y.; Wei, J.; Tian, Y. X.; Yan, S. Q. The Structure-Property Relationship of Manganese Oxides: Highly Efficient Removal of Methyl Orange from Aqueous Solution. *J. Mater. Chem. A* **2015**, *3*, 19000-19010.

(3) Meng, Y.; Song, W.; Huang, H.; Ren, Z.; Chen, S. Y.; Suib, S. L. Structure-Property Relationship of Bifunctional MnO_2 nanostructures: Highly Efficient, Ultra-Stable Electrochemical Water Oxidation and Oxygen Reduction Reaction Catalysts Identified in Alkaline Media. *J. Am. Chem. Soc.* **2014**, *136*, 11452-11464.

(4) Wang, J. F.; Deng, L. J.; Zhu, G.; Kang, L. P.; Lei, Z. B.; Liu, Z. H. Fluoride Anions-Assisted Hydrothermal Preparation and Growth Process of β-MnO_2 with Bipyramid Prism Morphology. *CrystEngComm* **2013**, *15*, 6682-6689.

(5) Jin, R.; Liu, H.; Guan, Y.; Zhou, J.; Li, G. Molten Salt Synthesis of Fluorine-Doped Mn_3O_4 Nanobelts as Anode Materials for Li-ion Batteries. *CrystEngComm* **2015**, *17*, 7717-7722.

(6) Duay, J.; Sherrill, S. A.; Gui, Z.; Gillette, E.; Lee, S. B. Self-Limiting Electrodeposition of Hierarchical MnO_2 and $M(OH)_2/MnO_2$ Nanofibril/Nanowires: Mechanism and Supercapacitor Properties. *ACS Nano* **2013**, *7*, 1200-1214.

(7) Tang, W.; Yao, M.; Deng, Y.; Li, X.; Han, N.; Wu, X.; Chen, Y. Decoration of One-Dimensional MnO_2 with Co_3O_4 Nanoparticles: a Heterogeneous Interface for Remarkably Promoting Catalytic Oxidation Activity. *Chem. Eng. J.* **2016**, *306*, 709-718.

(8) Chan, Y. L.; Pung, S. Y.; Sreekantan, S.; Yeoh, F. Y. Photocatalytic Activity of β-MnO_2 Nanotubes Grown on PET Fibre under Visible Light Irradiation. *J Exp Nanosci* **2016**, *11*, 603-618.

(9) Saha, S.; Pal, A. Microporous Assembly of MnO_2 Nanosheets for Malachite Green Degradation. *Sep Purif Technol* **2014**, *134*, 26-36.

(10) Kumar, N.; Sen, A.; Rajendran, K.; Rameshbabu, R.; Ragupathi, J.; Therese, H. A.; Maiyalagan, T. Morphology and Phase Tuning of α- and β-MnO_2 Nanocacti Evolved at

Varying Modes of Acid Count for their Well-Coordinated Energy Storage and Visible-Light-Driven Photocatalytic Behaviour. *RSC Adv.* **2017**, *7*, 25041-25053.

(11) Jia, J. B.; Zhang, P. Y.; Chen, L. Catalytic Decomposition of Gaseous Ozone over Manganese Dioxides with Different Crystal Structures. *Appl. Catal., B* **2016**, *189*, 210-218.

(12) Jana, S.; Pande, S.; Sinha, A. K.; Sarkar, S.; Pradhan, M.; Basu, M.; Saha, S.; Pal, T. A Green Chemistry Approach for the Synthesis of Flower-Like Ag-Doped MnO_2 Nanostructures Probed by Surface-Enhanced Raman Spectroscopy. *J. Phys. Chem. C* **2009**, *113*, 1386-1392.

(13) Hsu, Y. K.; Chen, Y. C.; Lin, Y. G.; Chen, L. C.; Chen, K. H. Birnessite-Type Manganese Oxides Nanosheets with Hole Acceptor Assisted Photoelectrochemical Activity in Response to Visible Light. *J. Mater. Chem.* **2012**, *22*, 2733-2739.

(14) Ramesh, M.; Nagaraja, H. S.; Rao, M. P.; Anandan, S.; Huang, N. M. Fabrication, Characterization and Catalytic Activity of α-MnO_2 Nanowires for Dye Degradation of Reactive Black 5. *Mater. Lett.* **2016**, *172*, 85-89.

(15) Yu, P.; Zhang, X.; Wang, D.; Wang, L.; Ma, Y. Shape-Controlled Synthesis of 3D Hierarchical MnO_2 Nanostructures for Electrochemical Supercapacitors. *Cryst. Growth Des.* **2009**, *9*, 528-533.

(16) Dawson, J. A.; Chen, H.; Tanaka, I. First-Principles Calculations of Oxygen Vacancy Formation and Metallic Behavior at a β-MnO_2 Grain Boundary. *ACS Appl. Mater. Interfaces* **2015**, *7*, 1726-34.

(17) Jia, J. B.; Zhang, P. Y.; Chen, L. The Effect of Morphology of α-MnO_2 on Catalytic Decomposition of Gaseous Ozone. *Catal Sci Technol* **2016**, *6*, 5841-5847.

(18) Balamurugan, S.; Rajalakshmi, A.; Balamurugan, D. Acetaldehyde Sensing Property of Spray Deposited β-MnO_2 Thin Films. *J. Alloys Compd.* **2015**, *650*, 863-870.

(19) Sanger, A.; Kumar, A.; Kumar, A.; Chandra, R. Highly Sensitive and Selective Hydrogen Gas Sensor using Sputtered Grown Pd Decorated MnO_2 Nanowalls. *Sens. Actuators, B* **2016**, *234*, 8-14.

(20) Alzahrani, S. A.; Al-Thabaiti, S. A.; Al-Arjan, W. S.; Malik, M. A.; Khan, Z. Preparation of Ultra Long α-MnO_2 and Ag@MnO_2 Nanoparticles by Seedless Approach and their Photocatalytic Performance. *J. Mol. Struct.* **2017**, *1137*, 495-505.

(21) Li, T. Q.; Wu, J. B.; Xiao, X.; Zhang, B. Y.; Hu, Z. M.; Zhou, J.; Yang, P. H.; Chen, X.; Wang, B.; Huang, L. Band Gap Engineering of MnO_2 Through *In Situ* Al-Doping for Applicable Pseudocapacitors. *RSC Adv.* **2016**, *6*, 13914-13919.

(22) Xing, X. J.; Yu, Y. P.; Xu, L. M.; Wu, S. X.; Li, S. W. Magnetic Properties of β-MnO_2 Thin Films Grown by Plasma-Assisted Molecular Beam Epitaxy. *J. Phys. Chem. C* **2008**, *112*, 15526-15531.

(23) Gao, J. J.; Jia, C. M.; Zhang, L. P.; Wang, H. M.; Yang, Y. H.; Hung, S. F.; Hsu, Y. Y.; Liu, B. Tuning Chemical Bonding of MnO_2 through Transition-Metal Doping for Enhanced CO Oxidation. *J. Catal.* **2016**, *341*, 82-90.

(24) Zhang, L. C.; Liu, Z. H.; Tang, X. H.; Wang, H. F.; Ooi, K. Synthesis and Characterization of β-MnO_2 Single Crystals with Novel Tetragonous Morphology. *Mater. Res. Bull.* **2007**, *42*, 1432-1439.

(25) Hu, P. P.; Huang, Z. W.; Hua, W. M.; Gu, X.; Tang, X. F. Effect of H_2O on Catalytic Performance of Manganese Oxides in NO Reduction by NH_3. *Appl. Catal., A* **2012**, *437*, 139-148.

(26) Huang, Z.-H.; Song, Y.; Feng, D.-Y.; Sun, Z.; Sun, X.; Liu, X.-X. High Mass Loading MnO_2 with Hierarchical Nanostructures for Supercapacitors. *ACS Nano* **2018**, *12*, 3557-3567.

(27) Shang, J.; Xie, B.; Li, Y.; Wei, X.; Du, N.; Li, H.; Hou, W.; Zhang, R. Inflating Strategy to Form Ultrathin Hollow MnO_2 Nanoballoons. *ACS Nano* **2016**, *10*, 5916-5921.

(28) Zhu, S.; Li, L.; Liu, J.; Wang, H.; Wang, T.; Zhang, Y.; Zhang, L.; Ruoff, R. S.; Dong, F. Structural Directed Growth of Ultrathin Parallel Birnessite on β-MnO_2 for High-Performance Asymmetric Supercapacitors. *ACS Nano* **2018**, *12*, 1033-1042.

(29) Moulai, F.; Fellahi, O.; Messaoudi, B.; Hadjersi, T.; Zerroual, L. Electrodeposition of Nanostructured γ-MnO_2 Film for Photodegradation of Rhodamine B. *Ionics* **2018**, *24*, 2099-2109.

(30) Truong, T. T.; Liu, Y.; Ren, Y.; Trahey, L.; Sun, Y. Morphological and Crystalline Evolution of Nanostructured MnO_2 and its Application in Lithium–Air Batteries. *ACS Nano* **2012**, *6*, 8067-8077.

(31) Toufiq, A. M.; Wang, F. P.; Javed, Q. U.; Li, Q. S.; Li, Y. Hydrothermal Synthesis of MnO_2 Nanowires: Structural Characterizations, Optical and Magnetic Properties. *Appl. Phys. A* **2014**, *116*, 1127-1132.

(32) Mattelaer, F.; Bosserez, T.; Ronge, J.; Martens, J. A.; Dendooven, J.; Detavernier, C. Manganese Oxide Films with Controlled Oxidation State for Water Splitting Devices through a Combination of Atomic Layer Deposition and Post-Deposition Annealing. *RSC Adv.* **2016**, *6*, 98337-98343.

(33) Merritt, A. R.; Rajagopalan, R.; Carter, J. D. Synthesis of Electro-Active Manganese Oxide Thin Films by Plasma Enhanced Chemical Vapor Deposition. *Thin Solid Films* **2014**, *556*, 28-34.

(34) Barreca, D.; Carraro, G.; Fois, E.; Gasparotto, A.; Gri, F.; Seraglia, R.; Wilken, M.; Venzo, A.; Devi, A.; Tabacchi, G.; Maccato, C. Manganese(II) Molecular Sources for Plasma-Assisted CVD of Mn Oxides and Fluorides: From Precursors to Growth Process. *J. Phys. Chem. C* **2018**, *122*, 1367-1375.

(35) Maccato, C.; Bigiani, L.; Carraro, G.; Gasparotto, A.; Seraglia, R.; Kim, J.; Devi, A.; Tabacchi, G.; Fois, E.; Pace, G.; Di Noto, V.; Barreca, D. Molecular Engineering of Mn^{II} Diamine Diketonate Precursors for the Vapor Deposition of Manganese Oxide Nanostructures. *Chem. Eur. J.* **2017**, *23*, 17954-17963.

(36) Barreca, D.; Gasparotto, A.; Tondello, E.; Sada, C.; Polizzi, S.; Benedetti, A. Nucleation and Growth of Nanophasic CeO_2 Thin Films by Plasma-Enhanced CVD. *Chem. Vap. Deposition* **2003**, *9*, 199-206.

(37) Simon, Q.; Barreca, D.; Bekermann, D.; Gasparotto, A.; Maccato, C.; Comini, E.; Gombac, V.; Fornasiero, P.; Lebedev, O. I.; Turner, S.; Devi, A.; Fischer, R. A.; Van Tendeloo, G. Plasma-Assisted Synthesis of Ag/ZnO Nanocomposites: First Example of Photo-Induced H_2 Production and Sensing. *Int. J. Hydrogen Energy* **2011**, *36*, 15527-15537.

(38) Liu, S.; Wang, Z.; Huang, Y.; Ni, Z.; Bai, J.; Kang, S.; Wang, Y.; Li, X. Fluorine Doping and Al_2O_3 Coating Co-modified $Li[Li_{0.20}Ni_{0.133}Co_{0.133}Mn_{0.534}]O_2$ as High Performance Cathode Material for Lithium-ion Batteries. *J. Alloys Compd.* **2018**, *731*, 636-645.

(39) Bigiani, L.; Barreca, D.; Gasparotto, A.; Sada, C.; Marti-Sanchez, S.; Arbiol, J.; Maccato, C. Controllable Vapor Phase Fabrication of F:Mn_3O_4 Thin Films Functionalized with Ag and TiO_2. *CrystEngComm* **2018**, *20*, 3016-3024.

(40) Carraro, G.; Gasparotto, A.; Maccato, C.; Bontempi, E.; Lebedev, O. I.; Turner, S.; Sada, C.; Depero, L. E.; Van Tendeloo, G.; Barreca, D. Fluorine Doped Fe_2O_3 Nanostructures by a One-Pot Plasma-Assisted Strategy. *RSC Adv.* **2013**, *3*, 23762-23768.

(41) Haddad, N.; Ben Ayadi, Z.; Mahdhi, H.; Djessas, K. Influence of Fluorine Doping on the Microstructure, Optical and Electrical Properties of SnO_2 Nanoparticles. *J. Mater. Sci. Mater. Electron.* **2017**, *28*, 15457-15465.

(42) Aydogu, S.; Coban, M. B.; Cabuk, G. Influence of Doping Fluorine on the Structural, Surface Morphological and Optical Properties of CdO Films. *Appl. Phys. A* **2017**, *123*, 409.

(43) Phulpoto, S.; Sun, J.; Qi, S.; Xiao, L.; Yan, S.; Geng, J. Tuning the Morphologies of Fluorine-Doped Tin Oxides in the Three-Dimensional Architecture of Graphene for High-Performance Lithium-Ion Batteries. *Nanotechnol.* **2017**, *28*, 395404.

(44) Sun, J.; Xiao, L.; Jiang, S.; Li, G.; Huang, Y.; Geng, J. Fluorine-Doped SnO_2@Graphene Porous Composite for High Capacity Lithium-Ion Batteries. *Chem. Mater.* **2015**, *27*, 4594-4603.

(45) Carraro, G.; Barreca, D.; Bekermann, D.; Montini, T.; Gasparotto, A.; Gombac, V.; Maccato, C.; Fornasiero, P. Supported F-Doped α-Fe_2O_3 Nanomaterials: Synthesis, Characterization and Photo-Assisted H_2 Production. *J. Nanosci. Nanotechnol.* **2013**, *13*, 4962-4968.

(46) Xiao, J.; Liu, P.; Liang, Y.; Li, H. B.; Yang, G. W. High Aspect Ratio β-MnO_2 Nanowires and Sensor Performance for Explosive Gases. *J. Appl. Phys.* **2013**, *114*, 073513.

(47) Schlossmacher, P.; Klenov, D. O.; Freitag, B.; von Harrach, H. S. Enhanced Detection Sensitivity with a New Windowless XEDS System for AEM Based on Silicon Drift Detector Technology. *Micros. Today* **2010**, *18*, 14-20.

(48) Gasparotto, A.; Barreca, D.; Bekermann, D.; Devi, A.; Fischer, R. A.; Fornasiero, P.; Gombac, V.; Lebedev, O. I.; Maccato, C.; Montini, T.; Van Tendeloo, G.; Tondello, E. F-

Doped Co_3O_4 Photocatalysts for Sustainable H_2 Generation from Water/Ethanol. *J. Am. Chem. Soc.* **2011**, *133*, 19362-19365.

(49) Barreca, D.; Bekermann, D.; Comini, E.; Devi, A.; Fischer, R. A.; Gasparotto, A.; Gavagnin, M.; Maccato, C.; Sada, C.; Sberveglieri, G.; Tondello, E. Plasma Enhanced-CVD of Undoped and Fluorine-Doped Co_3O_4 Nanosystems for Novel Gas Sensors. *Sens. Actuators, B* **2011**, *160*, 79-86.

(50) Pattern No. 024-0735, JCPDS (2000).

(51) Pattern No. 041-1442, JCPDS (2000).

(52) Tawil, S. N. M.; Norhidayah, C. A.; Sarip, N.; Kamaruddin, S. A.; Nurulfadzilah, A. R.; Miskon, A.; Sahdan, M. Z. Effect of Rare-Earth Gd Incorporation on the Characteristics of ZnO Thin Film. *J. Nanosci. Nanotechnol.* **2015**, *15*, 9212-9216.

(53) Zhang, A. M.; Wu, X. S.; Tang, S. L.; Zhou, S. M. Enhancement of Magnetic Anisotropy for L10-(001) FePt Films Grown on $SrTiO_3$ Substrate. *Chem. Phys. Lett.* **2016**, *654*, 135-138.

(54) Li, F.; Wangyang, P.; Zada, A.; Humayun, M.; Wang, B.; Qu, Y. Synthesis of Hierarchical Mn_2O_3 Microspheres for Photocatalytic Hydrogen Production. *Mater. Res. Bull.* **2016**, *84*, 99-104.

SYNOPSIS TOC

High purity nanomaterials based on β-MnO_2 were synthesized for the first time by plasma-assisted chemical vapor deposition from a diketonate-diamine Mn(II) complex with fluorinated ligands. The target compound enabled the obtainment of F-doped manganese oxide systems, with nano-organization evolving from columnar arrays to quasi-1D assemblies, and structural/magnetic features tunable as a function of the adopted growth temperature. Preliminary experiments evidenced their applicability in the photocatalytic degradation of aqueous pollutants triggered by visible light irradiation.